Title

A Turbulence Closure Study of the Flow and Thermal Fields in the Ekman Layer

Journal

Boundary-Layer Meteorology, 175(1)

ISSN

0006-8314

Authors

Braun, L
Younis, BA
Weigand, B

Publication Date

2020-04-01

DOI

10.1007/s10546-019-00495-8

Peer reviewed

Boundary-Layer Meteorology
https://doi.org/10.1007/s10546-019-00495-8

RESEARCH ARTICLE

A Turbulence Closure Study of the Flow and Thermal Fields in the Ekman Layer

Lukas Braun[1] · **Bassam A. Younis**[2] · **Bernhard Weigand**[1]

Received: 19 April 2019 / Accepted: 30 November 2019

Abstract
We assess the performance of turbulence closures of varying degrees of sophistication in the prediction of the mean flow and the thermal fields in a neutrally-stratified Ekman layer. The Reynolds stresses that appear in the Reynolds-averaged momentum equations are determined using both eddy-viscosity and complete differential Reynolds-stress-transport closures. The results unexpectedly show that the assumption of an isotropic eddy viscosity inherent in eddy-viscosity closures does not preclude the attainment of accurate predictions in this flow. Regarding the Reynolds-stress transport closure, two alternative strategies are examined: one in which a high turbulence–Reynolds–number model is used in conjunction with a wall function to bridge over the viscous sublayer and the other in which a low turbulence–Reynolds-number model is used to carry out the computations through this layer directly to the surface. It is found that the wall-function approach, based on the assumption of the applicability of the universal logarithmic law-of-the-wall, yields predictions that are on par with the computationally more demanding alternative. Regarding the thermal field, the unknown turbulent heat fluxes are modelled (i) using the conventional Fourier's law with a constant turbulent Prandtl number of 0.85, (ii) by using an alternative algebraic closure that includes dependence on the gradients of mean velocities and on rotation, and (iii) by using a differential scalar-flux transport model. The outcome of these computations does not support the use of Fourier's law in this flow.

Keywords Ekman layer · Prandtl number · Reynolds-stress closures · Similarity theory · Turbulent heat-flux closures

1 Introduction

Most turbulence closures in use for the prediction of environmental flows in general, and the atmospheric boundary layer (ABL) in particular, have been developed and calibrated with

✉ Bassam A. Younis
bayounis@ucdavis.edu

[1] Institut für Thermodynamik der Luft- und Raumfahrt, Universität Stuttgart, Stuttgart, Germany

[2] Department of Civil and Environmental Engineering, University of California - Davis, Davis, CA 95616, USA

Published online: 20 December 2019

reference to experimental data from simple, uni-directional two-dimensional shear flows in which complicating effects such as those arising from buoyancy, streamline curvature, or system rotation are entirely absent. In the Ekman layer–the boundary layer formed by pressure gradients induced in a rotating system and which is considered to be a realistic simpler representation of the ABL–the flow is three dimensional, the direction of the resultant velocity varies with height (the Ekman spiral) and, further, rotational effects appear explicitly in the equations governing the transport of momentum, and in the transport equations for the turbulent fluxes of momentum, heat, and contaminants. Thus some of the modelling assumptions inherent in these closures may no longer be valid in this more complex flow. One such assumption that is central to conventional turbulence closures, but whose validity in the more general ABL flow may be questionable, is that of Boussinesq in which the unknown Reynolds stresses are assumed to be proportional to the local mean rates of strain implying alignment of their respective directions. For this to be the case, the contributions of the convective and diffusive transport processes to the balances of the Reynolds stresses must be negligible compared to the processes of generation and dissipation. However, this condition is not always obtained (Kannepalli and Piomelli 2000). Moreover, in practical applications, the coefficient of proportionality, the eddy viscosity, is assumed to be isotropic when in fact measurements of three-dimensional shear flows show that this is not generally the case (Johnstone and Flack 1996). There is therefore a need to carefully evaluate the performance in the Ekman layer of some of the more commonly-used closures using reliable results obtained in recent direct numerical simulations (DNS) and experiments.

A number of studies on the assessment of turbulence closures for the Ekman layer have been reported in the literature. We confine attention here to those that used the more physically-based and widely-used 1.5- and 2.5-order turbulence closures. Of the former category, the $k-\epsilon$ model, with k being the turbulence kinetic energy (TKE) and ϵ its dissipation rate, appears to have received the most attention. Detering and Etling (1985), Andrén (1991), and Apsley and Castro (1997) found it necessary when using this model to modify the production term in the ϵ equation to improve the prediction of the wind profile in the ABL. In all these studies, the eddy viscosity was assumed to be isotropic. In contrast, Wirth (2010) postulated that the eddy viscosity is an anisotropic fourth-order tensor in three-dimensional space and derived an expression for it that produced good results for the Ekman spiral. Marlatt et al. (2012) used their DNS results to evaluate this model. They found that the closest agreement between the $k-\epsilon$ model results and the DNS data is obtained when the coefficient C_μ that enters into the calculation of the eddy viscosity is made a function of the turbulent Reynolds number. This coefficient was taken as constant in the previous studies, a practice that Marlatt et al. (2012) found to produce the least satisfactory agreement with the DNS results. We include the $k-\epsilon$ model in our assessment.

The notion of turbulent viscosity is dispensed within 2.5-order turbulence closures wherein the Reynolds stresses are obtained from the solution of a modelled differential transport equation for each component, a total of six for the Ekman layer. In this study, we evaluate two models of this category. These models have in common several of the approximations needed to close the exact equations for the Reynolds stresses but differ in one important respect: one is applicable only in the fully-turbulent region of the flow, thereby requiring the assumption that the universal logarithmic law-of-the-wall is valid so it can be used to bridge over the viscous sublayer, and another that is also applicable in the viscous sublayer thereby allowing for the simulations to be extended directly to the wall. Apart from determining the influence of each approach on the quality of the predictions, the results obtained with these models serve to show the extent to which the effects of convective and diffusive transport are important in such a flow. Furthermore, because all three models are solved using the same

computational tool, and their results tested against the same benchmark data, differences in their results can be attributed to their formulation with greater certainty.

We also consider the question of how best to model the turbulent transport of heat in the neutral Ekman layer, a topic that, despite its obvious importance, has received relatively less attention than that of the flow field. The usual approach to modelling the turbulent heat fluxes is to assume them to be proportional to the local gradients of mean potential temperature. The proportionality coefficient, the turbulent diffusivity, is in turn taken to be proportional to the turbulent viscosity via a turbulent Prandtl number typically taken to be constant. The assumption of a constant turbulent Prandtl number has been the subject of numerous studies, most recently by Li (2019) who found no evidence to support it. Here, we use this approach to modelling the heat fluxes and compare this with two other models that are entirely different in their formulation: one that is also algebraic in the heat fluxes but allows for the turbulent Prandtl number to vary depending on the details of the turbulence field, and another in which the fluxes are obtained from the solution of modelled differential transport equation, a total of three in the Ekman layer. The objective of these simulations is to place on record the performance of these three different modelling approaches and thus provide a basis for assessing their suitability for use in this flow.

While many of the features that pose the Ekman layer as an exacting test for turbulence closures are considered, we note that ABL flows are subject to complicating effects that are not considered here but whose presence can adversely affect the performance of these closures. Three complicating effects are worthy of note, these are: stable stratification, mean-flow unsteadiness and surface drag effects. The effects of stable stratification are to diminish the turbulence activity leading to reduction in the vertical turbulent fluxes of heat and momentum relative to the neutrally-stratified flow. A number of alternative approaches to sensitizing the turbulence closures to the effects of stable stratification have been proposed. Mauritsen et al. (2007), for example, proposed a model in which the TKE k, which is typically used in eddy-viscosity closures to obtain a characteristic turbulent velocity scale, is replaced by the total turbulence energy being the sum of k and the turbulent potential energy. The model's performance was assessed by comparisons with large-eddy simulations (LES) for neutral and stably-stratified cases where it was found to yield results that were indistinguishable from those of LES. Concerning the effects of mean-flow unsteadiness on the Ekman layer, large-eddy simulations by Momen and Bou-Zeid (2017) of a neutral flow with unsteady pressure forcing indicated that these effects are determined by the relative magnitudes of the time scales for the inertial and turbulence processes, and the pressure forcing. The results were used to test first- and 1.5-order turbulence closures which, for the case where the forcing and the turbulence time scales are comparable, were found to fail badly in capturing the changes wrought on the flow dynamics by virtue of the turbulence being out of equilibrium with the mean flow. The matter of how to account, in a turbulence closure, for the effects of surface drag produced by tall vegetative canopies was considered by Sogachev et al. (2012) who advanced a model based on extension of the equation for the turbulence length scale. The model proved successful in reproducing the effects of both vegetation and atmospheric stability. Consideration of how best to account for these complicating effects in the framework of the turbulence closures that are the focus of the present contribution is deferred to a future study.

2 Mathematical Formulation

2.1 Mean-Flow Equations

The coordinate system used is shown in Fig. 1, where the x- and y-axes are the horizontal coordinates and z is the vertical coordinate. The x-component of the freestream geostrophic velocity vector is $\mathbf{U_g} = (U_g, 0)$.

The flow is assumed to be horizontally homogeneous and hence all gradients in the y-direction vanish, and in accordance with the usual boundary-layer assumptions, diffusion is considered to be important only in the vertical direction. The flow is taken to be steady and the fluid (air) to be of constant properties. With these assumptions, the time-averaged equations governing the conservation of mass, momentum, and thermal energy (temperature) can be written as

$$\frac{\partial U}{\partial x} + \frac{\partial W}{\partial z} = 0, \tag{1}$$

$$U\frac{\partial U}{\partial x} + W\frac{\partial U}{\partial z} = \frac{\partial}{\partial z}\left(\nu\frac{\partial U}{\partial z} - \overline{uw}\right) - \frac{1}{\rho}\frac{\partial p}{\partial x} + fV, \tag{2}$$

$$U\frac{\partial V}{\partial x} + W\frac{\partial V}{\partial z} = \frac{\partial}{\partial z}\left(\nu\frac{\partial V}{\partial z} - \overline{vw}\right) - \frac{1}{\rho}\frac{\partial p}{\partial y} - fU, \tag{3}$$

$$U\frac{\partial \Theta}{\partial x} + W\frac{\partial \Theta}{\partial z} = \frac{\partial}{\partial z}\left(\frac{\nu}{Pr}\frac{\partial \Theta}{\partial z} - \overline{w\theta}\right). \tag{4}$$

In the above, U, V, and W are the velocity components in the x-, y-, and z-directions respectively, p is the time-averaged static pressure, Θ is the potential temperature, Pr is the molecular Prandtl number, ρ is the density, ν is the kinematic viscosity, and f is the Coriolis frequency,

$$f = 2\Omega\sin(\phi), \tag{5}$$

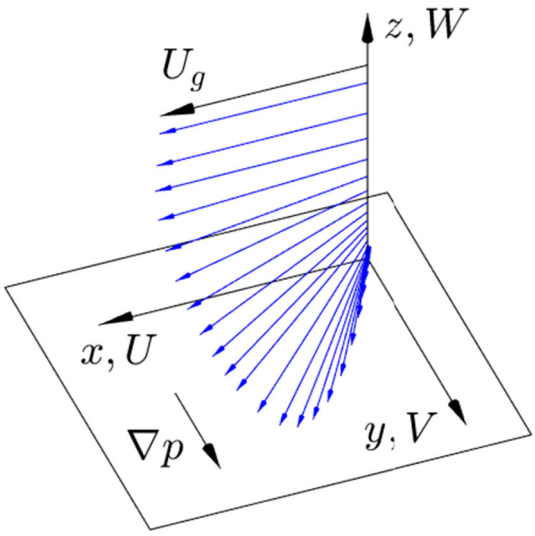

Fig. 1 Geostrophic coordinate system and a visualization of the computed Ekman spiral at 90° N

where Ω is the Earth's rotation rate and ϕ is the latitude. The pressure gradient in Eq. 3 is constant across the layer and is given by

$$\frac{\partial p}{\partial y} = -\rho f U_g. \tag{6}$$

In Eqs. 2–4, $-\overline{uw}$ and $-\overline{vw}$ are the components of the Reynolds-stress tensor that are responsible for the vertical transport of momentum by turbulence and $\overline{w\theta}$ is the vertical turbulent heat flux. These are unknown quantities that are determined using the turbulence closures given below.

2.2 The $k-\epsilon$ Model

The $k-\epsilon$ model utilizes Boussinesq's hypothesis in which the Reynolds stresses are assumed to be linearly proportional to the local rates of strain,

$$-\overline{u_i u_j} = K_m \left(\frac{\partial U_i}{\partial x_j} + \frac{\partial U_j}{\partial x_i} \right) - \frac{2}{3}\delta_{ij} k, \tag{7}$$

where K_m is the eddy viscosity.

In the Ekman layer, and to the boundary-layer approximations, Eq. 7 yields the following expressions for the momentum fluxes

$$\begin{aligned} -\overline{uw} &= K_m \frac{\partial U}{\partial z}, \\ -\overline{vw} &= K_m \frac{\partial V}{\partial z}. \end{aligned} \tag{8}$$

In the $k-\epsilon$ model, the eddy viscosity is obtained from

$$K_m = C_\mu \frac{k^2}{\epsilon}, \tag{9}$$

where ϵ is the dissipation rate of TKE. For the fully-developed Ekman layer, k and ϵ are obtained from the solution of the equations

$$U\frac{\partial k}{\partial x} + W\frac{\partial k}{\partial z} = \frac{\partial}{\partial z}\left[\left(\nu + \frac{K_m}{\sigma_k} \right) \frac{\partial k}{\partial z} \right] + P_k - \epsilon, \tag{10}$$

$$U\frac{\partial \epsilon}{\partial x} + W\frac{\partial \epsilon}{\partial z} = \frac{\partial}{\partial z}\left[\left(\nu + \frac{K_m}{\sigma_\epsilon} \right) \frac{\partial \epsilon}{\partial z} \right] + C_{\epsilon 1}\frac{\epsilon}{k} P_k - C_{\epsilon 2}\frac{\epsilon^2}{k}, \tag{11}$$

where P_k is the rate of production of k,

$$P_k = K_m \left(\left(\frac{\partial U}{\partial z} \right)^2 + \left(\frac{\partial W}{\partial z} \right)^2 \right). \tag{12}$$

The coefficients in this model are assigned their standard values, viz. $C_\mu = 0.09$, $\sigma_k = 1.0$, $\sigma_\epsilon = 1.3$, $C_{\epsilon 1} = 1.44$, $C_{\epsilon 2} = 1.92$ (Launder and Spalding 1972).

2.3 The Reynolds-Stress Transport Models

The exact equations governing the conservation of the Reynolds stresses $\overline{u_i u_j}$ form the basis of Reynolds-stress transport models (hereafter, RSM refers to the Reynolds-stress model). In rotating coordinates, these equations are given by

$$\overbrace{U_k \frac{\partial \overline{u_i u_j}}{\partial x_k}}^{\text{Convection: } C_{ij}} = \overbrace{-\left(\overline{u_i u_k}\frac{\partial U_j}{\partial x_k} + \overline{u_j u_k}\frac{\partial U_i}{\partial x_k}\right)}^{\text{Shear production: } P_{ij}} \overbrace{- 2\Omega_k \sin(\phi)\left(\overline{u_j u_m}\epsilon_{ikm} + \overline{u_i u_m}\epsilon_{jkm}\right)}^{\text{Rotation production: } G_{ij}}$$
$$\overbrace{+ \frac{\partial}{\partial x_k}\left[\nu \frac{\overline{\partial u_i u_j}}{\partial x_k} - \overline{u_i u_j u_k} - \frac{1}{\rho}\left(\overline{p' u_i}\delta_{jk} + \overline{p' u_j}\delta_{ik}\right)\right]}^{\text{Diffusion: } D_{ij}}$$
$$\overbrace{+ \overline{\frac{p'}{\rho}\left(\frac{\partial u_i}{\partial x_j} + \frac{\partial u_j}{\partial x_i}\right)}}^{\text{Pressure-strain: } \Phi_{ij}} \overbrace{- 2\nu \overline{\frac{\partial u_i}{\partial x_k}\frac{\partial u_j}{\partial x_k}}}^{\text{Dissipation: } \epsilon_{ij}}. \tag{13}$$

In Eq. 13, the terms representing convection, production by shear and rotation, and viscous diffusion are treated exactly as they appear in this equation. The remaining terms contain unknown correlations that are modelled as follows. In the diffusion term D_{ij}, the pressure diffusion term makes negligible contribution to the stress balances and is hence generally neglected (Wilcox 1993). The triple velocity correlations represent the process of diffusion due to velocity fluctuations, and are modelled according to the Daly and Harlow (1970) gradient-diffusion hypothesis

$$-\overline{u_i u_j u_k} = C_s \frac{k}{\epsilon}\overline{u_k u_l}\frac{\partial \overline{u_i u_j}}{\partial x_l}, \tag{14}$$

where C_k is a coefficient set equal to 0.22.

The fluctuating pressure rate-of-strain correlation term Φ_{ij} was modelled following Gibson and Launder (1978) and accounts for the ground effects on these correlations in the ABL

$$\Phi_{ij} = \Phi_{ij,1} + \Phi_{ij,2} + \Phi_{ij,1,w} + \Phi_{ij,2,w}. \tag{15}$$

The first two terms represent the effects on the fluctuating pressure field of turbulence fluctuations and of mean rates of strain. These are modelled as

$$\Phi_{ij,1} = -C_1 \frac{\epsilon}{k}\left(\overline{u_i u_j} - \frac{2}{3}\delta_{ij}k\right), \tag{16}$$

$$\Phi_{ij,2} = -C_2\left(P_{ij} - \frac{2}{3}\delta_{ij}P_k\right). \tag{17}$$

The last two terms represent the effects of a solid surface in damping the pressure fluctuations in its vicinity, and inhibit the transfer of energy to the turbulence fluctuation perpendicular to the surface. These terms are also modelled separately

$$\Phi_{ij,1,w} = C_{1,w}\frac{\epsilon}{k}\left(\overline{u_k u_m}n_k n_m \delta_{ij} - \frac{3}{2}\overline{u_k u_i}n_k n_j - \frac{3}{2}\overline{u_k u_j}n_k n_i\right) f_w, \tag{18}$$

$$\Phi_{ij,2,w} = C_{2,w}\left(\Phi_{km,2}n_k n_m \delta_{ij} - \frac{3}{2}\Phi_{ik,2}n_k n_j - \frac{3}{2}\Phi_{jk,2}n_k n_i\right) f_w, \tag{19}$$

where n_i is the unit vector normal to the wall and f_w is a function that reflects the strength of surface damping.

Gibson and Launder (1978) did not consider the contribution of the production by rotation term to the pressure-strain correlations. However, rotation-related terms do in fact appear in the exact equations for these correlations and hence their effects must also be accounted for

in the model for these correlations. Here, we adopt the proposals of Younis et al. (1998) by incorporating the production by rotation term in a manner analogous to Eq. 17

$$\Phi_{ij,3} = -C_3 \left(G_{ij} - \frac{2}{3}\delta_{ij} G_{ii} \right). \tag{20}$$

Following Gibson and Launder (1978) and Younis et al. (1998), the coefficients that appear in Eqs. 14–20 are assigned the values $C_1 = 1.8$, $C_2 = 0.6$, $C_3 = 0.6$, $C_{1,w} = 0.5$, $C_{2,w} = 0.3$, $C_s = 0.22$.

Since the fluid viscosity is absent from the exact equations for the fluctuating triple velocity correlations and the pressure-strain correlations, it may reasonably be assumed that the models for these correlations, which themselves are independent of viscosity, are valid across the entire range of turbulence Reynolds number. This does not apply to the last term in Eq. 13, which represents the rate at which $\overline{u_i u_j}$ is dissipated by viscous action. Here, we do expect that the model for ϵ_{ij} should reflect the DNS and experimental results that indicate that viscous dissipation is highly anisotropic in the viscosity-affected region of the flow but becomes isotropic in the high turbulent–Reynolds-number regions of the flow away from solid walls. A model that reflects the correct asymptotic behaviour of the dissipation rate term at both low- and high-turbulence Reynolds number is given by Kebede et al. (1985)

$$\epsilon_{ij} = \epsilon \left[\frac{2}{3}\delta_{ij} (1 - f_s) + f_s F \frac{\overline{u_i u_j} + \overline{u_i u_k} n_k n_j + \overline{u_j u_k} n_k n_i + \delta_{ij} \overline{u_k u_l} n_k n_l}{k} \right], \tag{21}$$

where n_i is again the unit vector normal to the surface. The function f_s in Eq. 21 is a function of the turbulence Reynolds number Re_t

$$f_s = \exp(-Re_t/40), \tag{22}$$

with $Re_t = k^2/(\nu\epsilon)$. Close to the wall, in the viscous sublayer, Re_t is low and f_s approaches a value of unity which eliminates the isotropic contribution and produces the correct anisotropy of the dissipation tensor. Farther away from the wall, Re_t is high and f_s approaches zero, and in this case, the model correctly obtains the expected isotropic dissipation result. The function F in Eq. 21, which is necessary to ensure that the trace of ϵ_{ij} yields the result $\epsilon_{ii} = 2\epsilon$, has the form

$$F = \left(1 + \frac{5}{2} \frac{\overline{u_k u_l}}{k} n_k n_l \right)^{-1}. \tag{23}$$

Differences between the high and low-Re_t models are also present in the equation from which ϵ is obtained. This equation can be written in a unified form applicable to both models as

$$U_l \frac{\partial \epsilon}{\partial x_l} = \frac{\partial}{\partial x_l} \left[\left(\nu \delta_{ml} + C_\epsilon \frac{k}{\epsilon} \overline{u_m u_l} \right) \frac{\partial \epsilon}{\partial x_m} \right] + C_{\epsilon 1} \frac{\epsilon}{k} P_k - C_{\epsilon 2} \frac{\epsilon \epsilon}{k} + C_{\epsilon 3} \nu \frac{k}{\epsilon} \overline{u_k u_l} \left(\frac{\partial^2 U_i}{\partial x_j \partial x_l} \right) \left(\frac{\partial^2 U_i}{\partial x_k \partial x_l} \right). \tag{24}$$

When Eq. 24 is used for the low-Re_t model calculations, it is more convenient from the standpoint of specifying the boundary conditions at the wall to solve an equation in which ϵ

Table 1 Coefficients of the ϵ equation

Model	C_ϵ	$C_{\epsilon 1}$	$C_{\epsilon 2}$	$C_{\epsilon 3}$	$C_{\epsilon 4}$
High Re_t	0.18	1.45	1.90	0	0
Low Re_t	0.18	$1.45\,(1 - f_s) + 2.0\,f_s$	1.90	0.3	1.0

is replaced everywhere by ϵ^*

$$\epsilon^* = \epsilon - 2C_{\epsilon 4}\nu\left(\frac{\partial\sqrt{k}}{\partial x_l}\right)^2, \tag{25}$$

where ϵ^* is the difference between ϵ and its value at the wall and can hence be set equal to zero there. The model coefficients are listed in Table 1.

2.4 Algebraic Turbulent Heat-Flux Models

2.4.1 Linear Model

In the linear model for the turbulent heat fluxes (Fourier's law), the heat fluxes are related to the local gradients of the potential temperature

$$-\overline{u_i\theta} = K_h\frac{\partial\Theta}{\partial x_i}, \tag{26}$$

where K_h is the turbulent diffusivity. In the fully-developed horizontally homogeneous Ekman layer, Eq. 26 gives the vertical turbulent heat flux as

$$-\overline{w\theta} = K_h\frac{\partial\Theta}{\partial z}. \tag{27}$$

The turbulent diffusivity is typically related to the turbulent viscosity via the turbulent Prandtl number (Pr_t) i.e.,

$$K_h = \frac{K_m}{Pr_t}, \tag{28}$$

where Pr_t is the turbulent Prandtl number which is typically assumed to be constant. Its value, deduced from laboratory experiments, ranges from 0.73 to 0.92 (Kays 1994). In the ABL, the precise value for Pr_t is the subject of ongoing research (see, for example, the recent review by Li 2019). In our work, we assign to this parameter the constant value of 0.85, which represents an average of the experimentally determined values.

It is worth noting here that Fourier's law aligns the directions of the turbulent heat fluxes with those of the temperature gradients. Thus in a flow, such as the present, where the only finite temperature gradient is in the z-direction, Eq. 26 indicates that only the vertical turbulent heat flux is finite–the horizontal flux components ($\overline{u\theta}$ and $\overline{v\theta}$) being identically zero. This feature of the linear turbulent flux model is of no consequence here since it is restricted to the case of neutral stratification. This would not be the case in vertical stratified flows (e.g. plumes) since the horizontal fluxes there enter into the expression for the buoyant rate of generation of TKE (Malin and Younis 1990).

Table 2 Coefficients of the non-linear algebraic heat flux model

C_{1t}	C_{2t}	C_{3t}	ξ	χ
0.03	0.21	0.105	0.2	4.0

2.4.2 Non-Linear Turbulent Flux Model

It will be seen in the next subsection that the exact equations for $\overline{u_i\theta}$ require the turbulent heat fluxes to explicitly depend on the gradients of mean velocity and on the rotation rate. A number of alternative proposals have been reported in the literature. We use the model proposed by Müller et al. (2015) because it has been extensively tested and because it incorporates an explicit dependence on the rotation rate. The model equation is

$$\begin{aligned} -\overline{u_i\theta} = \; & C_{1t}^{*}\frac{k^2}{\epsilon}\frac{\partial\Theta}{\partial x_i} + C_{2t}\frac{k}{\epsilon}\overline{u_iu_j}\frac{\partial\Theta}{\partial x_j} \\ & - C_{3t}\frac{k^2}{\epsilon^2}\left[\overline{u_iu_k}\left(\frac{\partial U_j}{\partial x_k} + \epsilon_{jmk}\Omega_m\sin(\phi)\right)\right. \\ & \left. + \overline{u_ju_k}\left(\frac{\partial U_i}{\partial x_k} + \epsilon_{imk}\Omega_m\sin(\phi)\right)\right]\frac{\partial\Theta}{\partial x_j}, \end{aligned} \tag{29}$$

with C_{1t}^{*} given by

$$C_{1t}^{*} = C_{1t}\left(1 - \exp(-A^{\chi}\,Pe_t^{\xi})\right), \tag{30}$$

where Pe_t $(= Pr\;Re_t)$ is the turbulent Peclet number and A is a parameter that depends on the second and third invariants of the Reynolds-stress anisotropy tensor. The values assigned to the model coefficients are listed in Table 2.

In the Ekman layer, Eq. 29 obtains the vertical heat flux as

$$-\overline{w\theta} = \overbrace{\frac{k^2}{\epsilon}\left(C_{1t}^{*} + C_{2t}\frac{\overline{w^2}}{k}\right)}^{K_h}\frac{\partial\Theta}{\partial z}. \tag{31}$$

Note that Fourier's law with constant turbulent Prandtl number can be recovered from Eq. 31 by setting $C_1^{*} = C_\mu/Pr_t$ and $C_{2t} = 0$. On the other hand, by retaining the assigned values for these coefficients, Eq. 31 can be recast in the manner of Eq. 28 with the eddy viscosity defined as in Eq. 9 to yield an expression for a variable turbulent Prandtl number

$$Pr_t = \frac{C_\mu}{C_{1t}^{*} + C_{2t}\overline{w^2}/k}. \tag{32}$$

A physical interpretation may be attached to Eq. 32: in the Ekman layer, the presence of a solid surface inhibits the transfer of turbulence energy from the normal-stress components where it is directly generated into $\overline{w^2}$, the component perpendicular to the surface. A reduction in the level of $\overline{w^2}$ compared to that in a free shear layer leads to a relatively higher value of Pr_t in the wall-bounded flow. This is consistent with experimental observations (e.g. Launder 1976).

2.5 Differential Transport Model for the Turbulent Fluxes

The exact equation describing the conservation of the turbulent heat fluxes in rotating coordinates is given by (see e.g. Younis et al. 2005)

$$\overbrace{U_k \frac{\partial \overline{u_i\theta}}{\partial x_k}}^{\text{Convection: } C_{i\theta}} = -\overbrace{\left(\overline{u_k u_i}\frac{\partial \Theta}{\partial x_k} + \overline{u_k\theta}\frac{\partial U_i}{\partial x_k}\right)}^{\text{Production: } P_{i\theta}} - \overbrace{2\epsilon_{ijk}\Omega_j \sin(\phi)\overline{u_k\theta}}^{\text{Rotation: } G_{i\theta}}$$
$$\overbrace{-\frac{\partial}{\partial x_k}\left[\overline{u_k u_i\theta} + \frac{\overline{p'\theta}}{\rho}\delta_{ik} - \Gamma\overline{u_i}\frac{\partial\theta}{\partial x_k} - \nu\theta\frac{\partial u_i}{\partial x_k}\right]}^{\text{Diffusion: } D_{i\theta}}$$
$$\overbrace{-(\Gamma+\nu)\frac{\partial\theta}{\partial x_k}\frac{\partial u_i}{\partial x_k}}^{\text{Dissipation: } \epsilon_{i\theta}} - \overbrace{\frac{p'}{\rho}\frac{\partial\theta}{\partial x_i}}^{\text{Correlations: } \pi_i}, \tag{33}$$

where Γ is the molecular thermal diffusivity. The convection term $C_{i\theta}$ and the production terms $P_{i\theta}$ and $G_{i\theta}$ are exact and in no need of modelling; $P_{i\theta}$ represents the production of $\overline{u_i\theta}$ due to turbulent interactions with the mean velocity temperature fields, and $G_{i\theta}$ represents additional contribution due to rotation Younis et al. (2012). The molecular diffusion part of the term $D_{i\theta}$ is also treated exactly but the diffusion by turbulence term is modelled by means of the gradient-diffusion hypothesis

$$-\overline{u_k u_i\theta} = C_\theta \frac{k}{\epsilon}\overline{u_k u_l}\frac{\partial\overline{u_i\theta}}{\partial x_l}, \tag{34}$$

where C_θ is a coefficient assigned the value of 0.15.

Following Gibson and Launder (1978) and Malin and Younis (1990), the fluctuating pressure–temperature correlations $\pi_{i\theta}$ are modelled as the sum of three terms

$$\begin{aligned}\pi_{i\theta} &= \pi_{i\theta,1} + \pi_{i\theta,2} + \pi_{i\theta,w}\\ &= -C_{1\theta}\frac{\epsilon}{k}\overline{u_i\theta} + C_{2\theta}(P_{i\theta} + G_{i\theta}) - C_{\theta,w}\frac{\epsilon}{k}\overline{u_i\theta}n_i n_k f_w.\end{aligned} \tag{35}$$

The third term on the right-hand side of Eq. 35 controls the strength of the wall correction in a manner analogous to that previously presented in connection with modelling the pressure-strain correlations. The coefficients in this equation are assigned their standard values viz. $C_{1\theta} = 2.85$, $C_{2\theta} = 0.55$, $C_{\theta,w} = 1.2$ (Malin and Younis 1990).

2.6 Solution Procedure

The governing equations were solved using the EXPRESS program (Younis 1987), which is a finite-volume solver for steady-state boundary-layer flows. Discretization of the convective and diffusive fluxes used the second-order accurate central-differencing scheme. A marching-integration strategy was used whereby the solutions were advanced in small forward steps in the x-direction (Fig. 1) from prescribed initial conditions until fully-developed conditions were attained. Iterations were performed at each step due to the strong coupling between the various equations. A non-uniform grid distribution was used in the vertical direction with the nodes being more concentrated in the near-wall region where the gradients of all dependent variables were greatest. In total, 53 grid nodes were used for the high-Re_t model and the $k-\epsilon$

model while, for the low-Re_t model, the number was increased to 160 in order to adequately resolve the flow in the viscous sublayer.

In the results that follow, the Coriolis frequency $f = 1.4 \times 10^{-4}\ \mathrm{s}^{-1}$, with the kinematic viscosity of air taken as $\nu = 1.46 \times 10^{-5}\ \mathrm{m}^2\ \mathrm{s}^{-1}$. With these values, the viscous Ekman layer depth $\delta_E\ (= \sqrt{2\nu/f})$, which describes the height at which viscous forces are dominant (Cushman-Roisin and Beckers 2010), is obtained as 0.54 m. The simulations were performed for a reference Reynolds number of $Re_f\ (= U_g\delta_E/\nu)$ of 1000 and a latitude of $\phi = 90°$ N, conditions that correspond to the DNS results of Marlatt et al. (2012) and Coleman et al. (1990) that will be used for model validation.

The boundary conditions applied at the surface depended on the choice of turbulence model. For the low-Re_t model, all the dependent variables were set equal to zero except for the temperature whose value there was set equal to $\Theta_w = 288.2$ K. With the high-Re_t model, the first computational grid node was located outside the viscous sublayer where it was assumed that the modulus of the resultant velocity, $Q = \sqrt{U^2 + V^2}$, obeys the universal law-of-the-wall

$$Q^+ = \frac{Q}{Q_\tau} = \frac{1}{\kappa}\ln\left(z^+\right) + C, \tag{36}$$

where Q_τ is the friction velocity $(= \sqrt{\tau_w/\rho})$ and $z^+ = Q_\tau z/\nu$. The von Kármán constant κ, and C are assigned their usual values of 0.41 and 5.0, respectively. Furthermore, at the same node, the vertical gradients of the Reynolds stresses and heat fluxes were set equal to zero, consistent with the assumption of a constant-stress region, while the value of dissipation was set equal to the rate of production of TKE.

In the freestream, the x-component of the velocity vector is set equal to U_g and the temperature there assigned the constant value $\Theta_g = 298.2$ K. The overall temperature difference of 10 K is sufficiently small for the air properties to remain constant and for stratification effects to be negligible. The dissipation rate and all components of the Reynolds-stress tensor were set equal to zero, and when the differential heat flux model was used, the turbulent heat fluxes were also set to zero there.

At the inlet, the mean velocity components were prescribed in accordance with the analytical solutions for laminar flow (Cushman-Roisin and Beckers 2010) viz.,

$$U = U_g\left(1 - \exp(-z/\delta_E)\cos\frac{z}{\delta_E}\right), \tag{37}$$

$$V = U_g\exp(-z/\delta_E)\sin\frac{z}{\delta_E}. \tag{38}$$

The mean temperature profile is assumed to be similar to the mean streamwise velocity profile viz.,

$$\Theta = \Theta_w + \left(\Theta_g - \Theta_w\right)\frac{U}{U_g}. \tag{39}$$

The profiles of the turbulence parameters were prescribed based on the experimental correlations of Schlichting and Gersten (2006). Thus the turbulent shear stress -$\overline{uw}$ was assumed to vary linearly with distance from the surface until reaching a maximum value of Q_τ^2 at $z^+ = 10$ and then to decrease linearly to vanish at the free stream. The TKE k was then obtained from the structure parameter $-\overline{uw}/k = 0.3$ and the normal stresses obtained in the same proportion to k as in a flat-plate boundary layer, i.e. $\overline{u^2}/k = 1.0$, $\overline{v^2}/k = 0.6$ and $\overline{w^2}/k = 0.4$. The dissipation rate ϵ was deduced from the eddy-viscosity relationship Eq. 9.

3 Results and Discussion

To compare with experimental and DNS results, it was necessary to ensure that the computations were performed along sufficient length to obtain profiles that are self-similar and independent of the profiles prescribed at the inlet. Two parameters were chosen to test for the attainment of self-similarity: the skin-friction coefficient c_f, being representative of the state of the flow field, and, for the thermal field, the Stanton number St, which is the ratio of the heat transferred into the boundary layer to its thermal capacity. These parameters are defined as

$$c_f = 2\left(\frac{Q_\tau}{U_g}\right)^2, \tag{40a}$$

$$St = \frac{Nu_x}{Re_x\, Pr}, \tag{40b}$$

where Re_x $(= x\, U_g/\nu)$ is the Reynolds number and Nu_x is the Nusselt number

$$Nu_x = -\frac{(\partial\Theta/\partial z)_{z=0}}{\left(\Theta_w - \Theta_g\right)/x}. \tag{41}$$

Since the computations were started from profiles that were not in equilibrium, it is to be expected that Nu and Re would initially vary with streamwise distance until equilibrium is established and these parameters attain constant values. In such conditions, the Reynolds analogy between the turbulent transfer of heat and momentum is expected to apply. A modified form of the Reynolds analogy, and one which is applicable to fluids with non-unity Prandtl number, is the Chilton–Colburn analogy, which indicates that when both the flow and thermal fields have attained equilibrium, then $Pr^{2/3} St = c_f/2$. Figure 2 shows the streamwise variation c_f and St, and of their ratio in line with the Chilton–Colburn analogy. It is immediately evident that the effects of the assumed inlet profiles persist over a significant development length until equilibrium is achieved wherein c_f and St become constant and their ratio becomes approximately equal to one, thereby providing an independent confirmation of the modified analogy. Once equilibrium is achieved, then the predicted profiles of velocity, temperature and turbulent heat and momentum fluxes, appropriately non-dimensionalized, cease to change with further streamwise development.

3.1 Mean Velocity Profiles

The predicted mean velocity profiles are shown in Fig. 3, where they are compared with the DNS results of Marlatt et al. (2012). The velocity components in the streamwise (U) and lateral (V) directions are non-dimensionalized with the freestream geostrophic velocity component U_g. The vertical distance is non-dimensionalized by the turbulent Ekman layer depth $\delta_\tau = Q_\tau/f$. All model simulations predict a maximum of U greater than U_g. This supergeostrophic region is also evident in the DNS results of Marlatt et al. (2012) and in the measurements performed by Caldwell et al. (1972) and Sous and Sommeria (2012). It is considered a characteristic feature of the Ekman layer that arises because the pressure gradient in the y-direction that induces the lateral flow is constant with height while the Coriolis force increases with it. This, together with reduction in friction with distance from the wall, produces the observed supergeostrophic peak. With further increase in height, the lateral velocity component V decreases due to the balance between the Coriolis force and the pressure gradient. At the top of the Ekman layer, the geostrophic balance results

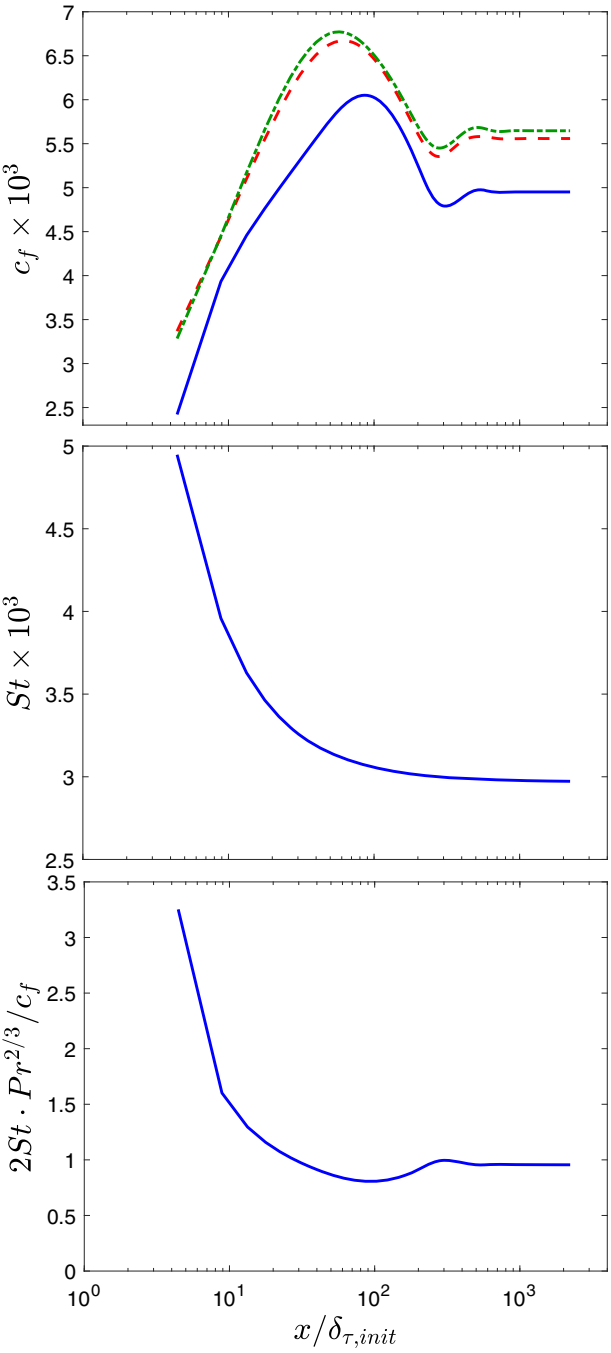

Fig. 2 Streamwise development of skin friction coefficient c_f, Stanton number St, and their ratio. low-Re_t model; high-Re_t model; $k-\epsilon$ model

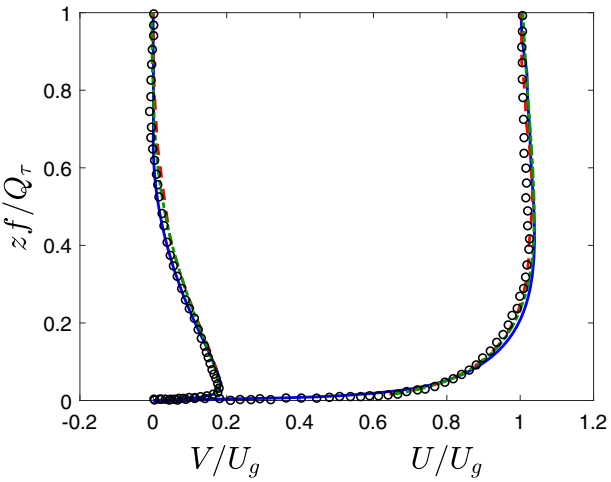

Fig. 3 Mean velocity profiles as a function of non-dimensional height. ——— low-Re_t model; - - - - - high-Re_t model; -·-·-·- $k-\epsilon$ model; ◯ DNS of Marlatt et al. (2012)

in an extinction of the V-component and a flow parallel to the geostrophic velocity with speed U_g. Overall, the V profile resembles that of a wall jet. The low-Re_t model yields predictions that are close to the DNS of Marlatt et al. (2012), with a slight overprediction of the streamwise velocity component U. The high-Re_t model and the $k-\epsilon$ model obtain almost indistinguishable results.

Figure 4 shows the predicted mean velocity profiles in the form of a hodograph. Also shown there are the DNS results of Coleman et al. (1990) and, for interest, the laminar solutions (Eqs. 37, 38). The low-Re_t model again shows good agreement with the DNS results, especially near the wall. The $k-\epsilon$ model prediction is close to the high-Re_t model and both predictions agree well with the DNS; there is only a slight underprediction of V near the wall. The high-Re_t model and the $k-\epsilon$ model fail to provide a simulation of the whole Ekman hodograph, because the first node is placed in the logarithmic layer, at z^+ of around 25, while the low-Re_t model is applied directly to the surface.

The model predictions of the resultant mean velocity magnitude Q are plotted in wall coordinates in Fig. 5 where they are compared with the DNS results of Marlatt et al. (2012). Also shown there are the standard profiles for the viscous sublayer ($Q^+ = z^+$) and for the fully-turbulent flow (Eq. 36). The low-Re_t model follows the viscous sublayer profile until $z^+ \approx 6$ and agrees well with the DNS until $z^+ \approx 30$. For $30 < z^+ < 200$, the non-dimensional velocity Q^+, obtained by means of the low-Re_t model, still describes a logarithmic region but one with somewhat different slope and intercept than Eq. 36 and the DNS. The reason can be found in an underprediction of the friction velocity Q_τ (see Table 3). The high-Re_t model result, also shown in Fig. 5, indicates that at $z^+ \approx 25$, the value for Q^+ is fixed to the logarithmic law-of-the-wall. The high-Re_t model and the $k-\epsilon$ model reach nearly the same simulation results for Q^+. Both models follow fairly closely to both the law-of-the-wall and to the DNS, since the absolute friction velocity is obtained by means of the logarithmic law-of-the-wall and the mean profiles of U and V are correctly predicted (see Fig. 4). In summary, although Q^+, obtained with the low-Re_t model, partially deviates from the DNS and empirical predictions, it still predicts the characteristic velocity profile composed of a viscous sublayer, a logarithmic layer and a wake region, while Q^+, obtained

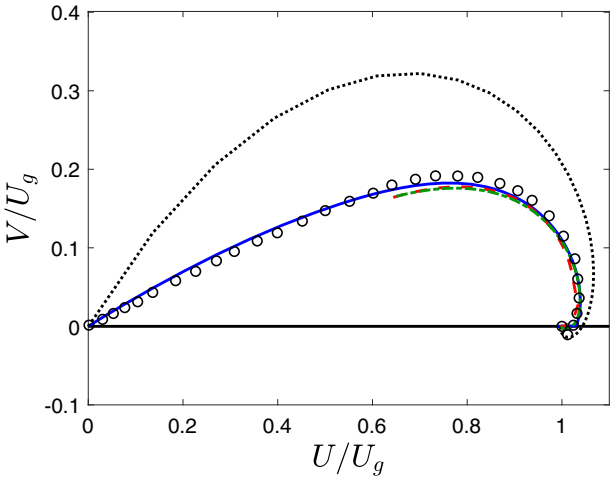

Fig. 4 Ekman spiral as a non-dimensional hodograph. ——— low-Re_t model; - - - - - high-Re_t model; -·-·- $k-\epsilon$ model; ◯ DNS of Coleman (1999); ····· laminar solution

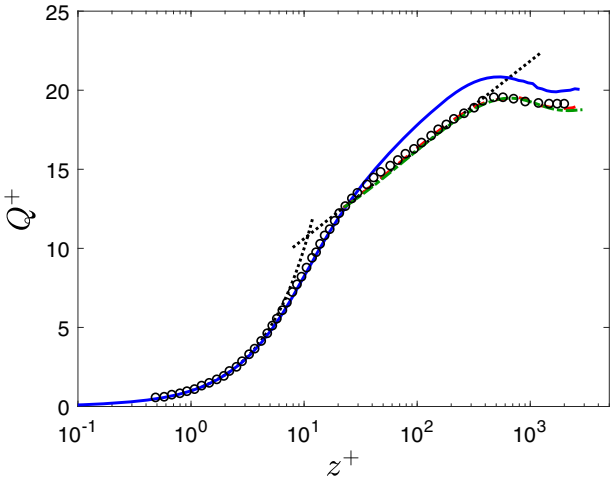

Fig. 5 Resultant mean velocity profile in terms of wall coordinates. ——— low-Re_t model; - - - - - high-Re_t model; -·-·- $k-\epsilon$ model; ◯ DNS of Marlatt et al. (2012); ····· $Q^+ = z^+$ and $Q^+ = 1/0.41\ln(z^+) + 5$

by means of the high-Re_t model and the $k-\epsilon$ model, can only predict a characteristic logarithmic region and a wake region.

3.2 The Reynolds Stresses

Figure 6 compares the predicted profiles of the Reynolds stresses with the DNS results of Marlatt et al. (2012) and the atmospheric measurements of Brost et al. (1982). Brost et al. (1982) scaled the vertical height by the inversion height z_i. With reference to Andrén

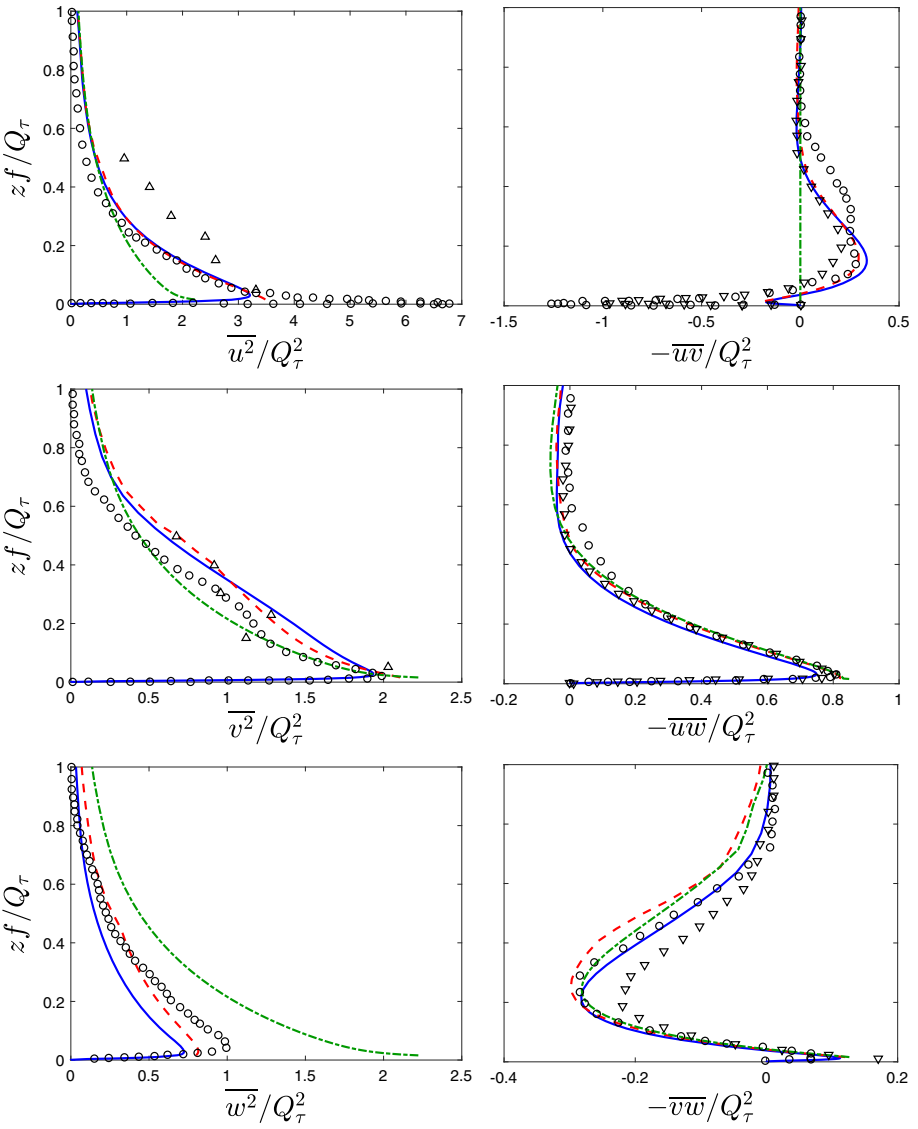

Fig. 6 Normal (left) and shear (right) Reynolds stresses. ——— low-Re_t model; - - - - high-Re_t model; -·-·- $k-\epsilon$ model; ◯ DNS of Marlatt et al. (2012); ▽ DNS of Coleman (1999); △ atmospheric data of Brost et al. (1982)

(1991), who relied on observations, the atmospheric data are rescaled by using the assumption $z_i = 0.4Q_\tau/f$.

In general, the normal stresses exhibit a broadly similar behaviour. Until the streamwise velocity component U reaches the geostrophic wind speed, $\overline{u^2}$ is dominant, whereas $\overline{v^2}$ becomes dominant in the supergeostrophic region. As also mentioned in Marlatt et al. (2012), the surface impedes the vertical fluctuations, which is evident in the low value of $\overline{w^2}$ compared to the other normal stresses.

The normal stresses $\overline{u^2}$ and $\overline{w^2}$ obtained by Marlatt et al. (2012) reach a maximum in the viscous sublayer, whereas the normal stresses obtained with the low-Re_t model reach a maximum in the logarithmic region at about $z^+ \approx 35$. The normal stresses obtained with the high-Re_t model and the $k-\epsilon$ model both reach their maximum at the first node, fixed at $z^+ \approx 25$. The $k-\epsilon$ model fails to closely match DNS results partly because, being based on the Boussinesq assumption and the flow being fully developed, it predicts all three components of normal stress to be equal. The low- and high-Re_t model achieve similar results for $z^+ > 25$ and both models underpredict the maximum values of $\overline{u^2}$ and $\overline{w^2}$. However, the predicted maximum of $\overline{v^2}$ is very close to the DNS of Marlatt et al. (2012). Both Reynolds-stress transport models therefore provide generally satisfactory results compared to DNS data. As the normal stress results are in the range of the atmospheric data of Brost et al. (1982), the current simulation seems to reproduce real atmospheric conditions.

The turbulent shear stresses are compared with the DNS results of Marlatt et al. (2012) and Coleman (1999) in Fig. 6. The maximum value of $-\overline{uw}$ near the wall is reproduced best by means of the high-Re_t model and the $k-\epsilon$ model. However, the profile obtained with the $k-\epsilon$ model deviates from the DNS results farther away from the wall. The low-Re_t model underpredicts the maximum of $-\overline{uv}$ provided by Marlatt et al. (2012) and Coleman (1999). However, the location of the maximum at $z^+ \approx 16$ corresponds with Marlatt et al. (2012) (maximum at $z^+ \approx 12$). In contrast, the $k-\epsilon$ model predicts this component of shear stress to be zero everywhere as a consequence of $\partial U/\partial y$ and $\partial V/\partial x$ being zero in this horizontally homogeneous, fully-developed flow. The shear stress $-\overline{vw}$ profile obtained with the low-Re_t model provides a very good approximation of the DNS results of Coleman (1999), besides an underprediction of the near-wall minimum value. The change of sign of $-\overline{uv}$ correlates with $-\overline{vw}$ at $z^+ \approx 50$ and appears where the lateral velocity component V reaches its maximum. This location is close to the prediction of Marlatt et al. (2012) at $z^+ \approx 58$. The low-Re_t model and the $k-\epsilon$ model results are similar for $-\overline{vw}$, while the high-Re_t model deviates from both models for $0.2 < zf/Q_\tau < 0.5$. The low-Re_t model predicts the location of the Reynolds stress peaks correctly and the obtained profiles agree with the DNS. However, the near-wall peak values of $\overline{u^2}$, $\overline{w^2}$, and $-\overline{uv}$ are underpredicted. The stress profiles, obtained with the high-Re_t model are close to the profiles obtained with the low-Re_t model. Thus if detailed predictions of the Reynolds-stress profiles in the viscous sublayer are not of interest, there would be little advantage in using the low-Re_t model in preference to the high-Re_t model.

An interesting result to emerge from the present simulation concerns the lateral velocity component V, specifically its vertical gradient $\partial V/\partial z$ and the turbulent shear-stress component $-\overline{vw}$ that enters into its equation (Eq. 3). In a two-dimensional boundary layer, these two quantities are of the same sign as suggested by the Boussinesq assumption. In the Ekman layer, the vertical profile of V resembles that of a wall jet (Fig. 3). Due to turbulent transport, the location where $-\overline{vw} = 0$ in the wall jet does not coincide with the location where $\partial V/\partial z = 0$ but lies in-board of it, closer to the surface (Irwin 1973). This is also obtained in our simulations with the Reynolds-stress models where the shear stress becomes zero at $zf/Q_\tau = 0.040$ while the velocity gradient becomes zero at a value of 0.046. The $k-\epsilon$ model obtains the two locations as coincident but this does not appear to have caused significant errors in its results.

A characteristic of three-dimensional flows such as the Ekman layer is that the angles that the resultants of the velocity, the velocity gradients and the shear stress make with the x-axis are not equal and, further, they vary in the vertical direction. These angles are defined as

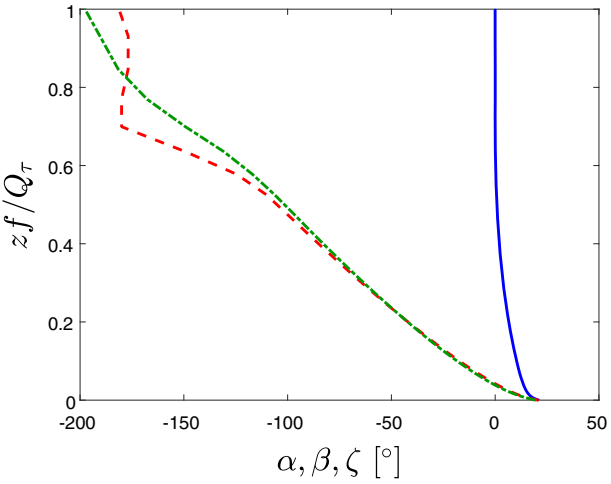

Fig. 7 Flow angles as predicted with the low-Re_t model. shear-stress angle α; velocity gradient angle β; resultant velocity angle ζ

shear stress angle

$$\alpha = \tan^{-1}\left(\frac{\overline{vw}}{\overline{uw}}\right), \tag{42}$$

velocity gradient angle

$$\beta = \tan^{-1}\left(\frac{\frac{\partial V}{\partial z}}{\frac{\partial U}{\partial z}}\right), \tag{43}$$

and wind direction angle

$$\zeta = \tan^{-1}\left(\frac{V}{U}\right). \tag{44}$$

Here, these angles are obtained with the low-Re_t model, since the high-Re_t model and the $k-\epsilon$ model do not resolve the viscous sublayer and hence cannot provide values at the surface. As can be seen in Fig. 7, the wind direction angle ζ starts at the wall with a value similar to the other two angles. With increasing height, ζ decreases due to a growing Coriolis force until finally approaching the value zero since the flow is parallel to the x-axis and the lateral velocity component V is zero. Up until a height of $zf/Q_\tau \approx 0.7$ the shear-stress angle α and the velocity-gradient angle β nearly linearly spiral with z, and at the same same time α and β produce very similar results until $zf/Q_\tau \approx 0.4$. For $zf/Q_\tau > 0.4$, however, β becomes larger than α and the angles deviate from each other by up to 30 degrees. A similar behaviour is obtained in the DNS results of Coleman et al. (1990). The $k-\epsilon$ model assumption of a proportionality between Reynolds stresses and mean velocity gradients implies equality of α and β, which is a reasonable assumption close to the surface but is not generally true.

There are two important parameters that characterize the Ekman layer, the geostrophic drag coefficient Q_τ/U_g and the surface shear-stress angle α_w. These are evaluated for different Reynolds numbers and by means of the similarity theory of Spalart (1989) extrapolated to larger Reynolds numbers. The parameters are important, since they express the magnitude and the direction of the shear stress at the surface. The different model predictions are compared with DNS results in Table 3. Note that $\alpha_w = 45°$ for the laminar Ekman layer. The geostrophic drag coefficient obtained with the low-Re_t model deviates between 4–7% from

Table 3 Geostrophic drag coefficient Q_τ/U_g and surface shear-stress angle α_w in comparison with DNS results ($\phi = 90°$)

Case	Re_f	Q_τ/U_g	α_w°
$k-\epsilon$ model	1000	0.0532	-
High Re_t model	1000	0.0528	-
Low Re_t model	1000	0.0499	19.41
Marlatt et al. (2012)	1000	0.0520	18.56
Miyashita et al. (2006)	1140	0.0521	19.40
Coleman (1999)	1000	0.0530	19.00
Spalart et al. (2008)	1000	0.0535	19.36

the DNS data, the high-Re_t model and the $k-\epsilon$ model only 1–2%. These results confirm that the high-Re_t model and the $k-\epsilon$ model align more with the logarithmic law-of-the-wall than the low-Re_t model. As the wall modelling for the high-Re_t model does not provide any values for the shear-stress angle at the surface, there is no α_w result for the $k-\epsilon$ model and the high-Re_t model. α_w, obtained by means of the low-Re_t model, differs from the DNS results between 1–5%.

We next consider the model predictions of α_w and Q_τ/U_g for values of Re_t in the range 730–4000. The results are presented in Fig. 8 where they are compared with the DNS results of Coleman (1999), Coleman et al. (1990), Spalart et al. (2008) and Miyashita et al. (2006). The high-Re_t model results for Q_τ/U_g show a reasonable development, compared to the DNS data. However, the slope of the profile is higher. The obtained values of Q_τ/U_g by means of the low-Re_t model are shifted downwards, but the development for Reynolds number of $Re_f \geq 1000$ is parallel to the DNS results. The low-Re_t model results show an interesting development for Reynolds numbers of $Re_f < 1000$, as Q_τ/U_g rapidly decreases, whereas α_w rapidly increases. After investigating the behaviour of other quantities, such as the mean velocity components and the Q profile in terms of wall coordinates, an Ekman layer with a laminar-like behaviour can be discovered. That corresponds with the results of Miyashita et al. (2006), where the authors cannot observe a logarithmic region for $Re_f = 600$, but an emerging logarithmic region at $Re_f = 775$. The results of α_w for $Re_f \geq 1000$, obtained with the low-Re_t model, are close to the DNS results.

3.3 Similarity Theory

The present simulations were performed at a Reynolds number of $Re_f = 1000$ so that the results can be compared with those in the established literature (Table 3). This value is undoubtedly lower than that encountered in actual ABL conditions. However, as Marlatt et al. (2012) and Coleman (1999) suggest, Ekman-layer simulations at low Reynolds numbers can still be useful and representative of ABL conditions as long as the computed mean velocity profiles exhibit a logarithmic region. As shown in Fig. 5, this requirement is satisfied by the present predictions. Given the results at low Reynolds numbers, the goal is to be able to extrapolate the two important Ekman-layer parameters, Q_τ/U_g and α_w, to higher Reynolds numbers that are more representative of actual ABL conditions. The ability to do this would render the simulations at low Reynolds numbers useful for the purposes of weather/climate predictions at high Reynolds numbers. Csanady (1967) developed a similarity theory that enables this extrapolation. The theory is founded on the existence of the logarithmic law-of-the-wall. The law is applied to three dimensions, which involves the surface shear stress

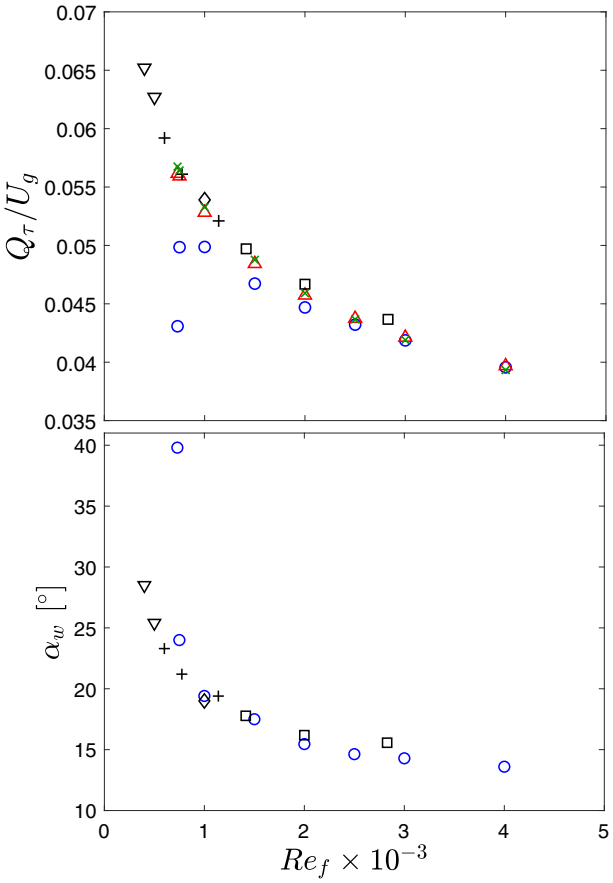

Fig. 8 Variation of the geostrophic drag coefficient Q_τ/U_g (top) and surface shear-stress angle α_w with Reynolds number. ◯ low-Re_t model; △ high-Re_t model; $\times k-\epsilon$ model; + DNS of Miyashita et al. (2006); ▽ DNS of Coleman et al. (1990); ◊ DNS of Coleman (1999); □ DNS of Spalart et al. (2008)

α_w. Spalart (1989) found that Csanady (1967) theory did not agree with simulation at low Reynolds numbers ($Re_f = 500-767$) and proposed a modification that involved the addition of a higher-order term and an additional equation

$$A = \frac{U_g}{Q_\tau}\sin\theta_w, \tag{45}$$

$$B = \frac{U_g}{Q_\tau}\cos\theta_w + \frac{2}{\kappa}\ln\frac{U_g}{Q_\tau} - \frac{2}{\kappa}Re_f + \frac{1}{\kappa}\ln 2, \tag{46}$$

$$\theta_w = \alpha_w + \frac{2C_5}{Re_f^2}\left(\frac{U_g}{Q_\tau}\right)^2. \tag{47}$$

Equations 45 and 46 represent Csanady (1967) theory but with the actual surface shear angle α_w replaced by a shifted angle θ_w as defined by Eq. 47. A number of coefficients are involved, of which the von Kármán constant κ is assigned its usual value of 0.41. The remaining three constants (A, B, and C_5) are obtained by substituting the DNS results into

Table 4 Determination of the similarity theory constants A and B ($\kappa = 0.41$ and $C_5 = -52$)

Re_f	Q_τ/U_g	$\alpha_w{}^\circ$	$\theta_w{}^\circ$	A	B
2000	0.04469	15.46	15.45	5.960	1.342
2500	0.04322	14.63	14.62	5.841	1.237
3000	0.04187	14.29	14.28	5.893	1.259
4000	0.03956	13.60	13.60	5.942	1.557
			Average	5.909	1.349

Eqs. 45–47. Coleman et al. (1990), using the DNS results for $Re_f = 400$ and $Re_f = 500$ and $C_5 = -52$, obtained the extrapolated results shown in Fig. 9. We revisit this approach by using the results from our low-Re_t model to evaluate the constants A and B only now with the benefit of having data from much higher values of Re_f than those used by Coleman et al. (1990). The outcome of this re-evaluation is presented in Table 4. Note that according to Coleman (1999), the modification of the surface shear stress angle, θ_w, is needed when $Re_f < 5000$, which is the case here. Subsequently, A and B are calculated by Eqs. 45 and 46 at each Reynolds number. As can be seen in Table 4, the obtained values are not very different from each other and, when averaged, yield the values of $A = 5.91$ and $B = 1.35$.

In Fig. 9, the extrapolated values of the geostrophic drag coefficient Q_τ/U_g and the surface shear angle α_w as obtained using the averaged values of A and B and those of Coleman et al. (1990) are compared. In presenting the results obtained with our model, a continuous line is used to designate the range of Re_f values used to evaluate A and B, and a dashed line to show the range over which the results have been extrapolated. We subsequently performed calculations at three significantly higher values of Re_f viz. 10, 000, 20, 000, and 40, 000 to explore the extent to which the model results agreed with similarity theory together with the averaged values of A and B. As can be seen from Fig. 9, the results are quite close which suggests that similarity theory can yield useful results despite the many assumptions invoked in its formulation.

3.4 Mean Temperature Profile

The predicted mean temperature profiles are shown in Fig. 10 as a function of non-dimensional height. Since, for air, $Pr < 1$, the thermal boundary layer is slightly thicker than the momentum boundary layer and hence the mean temperature profile and the turbulent heat fluxes are presented for $0 \le zf/Q_\tau \le 1.5$. The difference between the explicit algebraic model and the differential transport model is insignificant. However, the mean temperature profile obtained with Fourier's law departs from the other two models by providing smaller temperature values for $zf/Q_\tau > 0.06$. This result is entirely due to assigning the turbulent Prandtl number a constant value of 0.85. By assigning the higher value of 1 implied by the alternative models, all the predicted temperature profiles become virtually indistinguishable from each other.

Figure 11 shows the mean temperature profiles plotted in wall coordinates in order to compare the simulation results with a law-of-the-wall for temperature, proposed by Duponcheel et al. (2014)

$$\Theta^+ = \frac{\Theta - \Theta_w}{\Theta_\tau} = \frac{Pr_t}{\kappa} \ln\left(1 + \frac{Pr}{Pr_t}\kappa\, z^+\right), \tag{48}$$

where the friction temperature Θ_τ is defined as

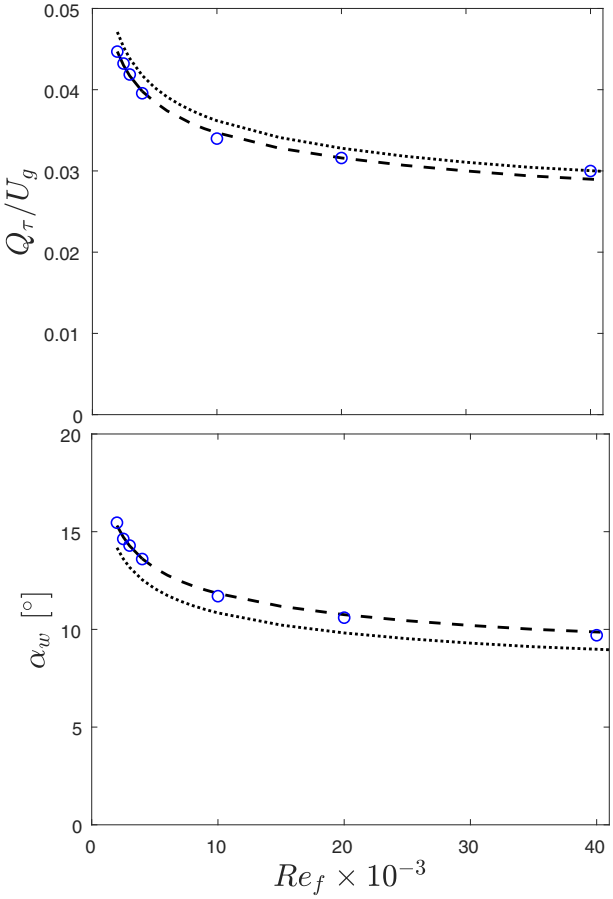

Fig. 9 Similarity theory and low-Re_t model results for the variation of geostrophic drag coefficient (top) and surface shear stress angle with Re_f. Present values (Table 4): ——— fitted curve; - - - - - extrapolated curve. Coleman et al. (1990) values of A and B: ····· ◯ low-Re_t model predictions

$$\Theta_\tau = \frac{\lambda \left(\frac{\partial \Theta}{\partial z}\right)_{z=0}}{\rho c_p Q_\tau}. \tag{49}$$

Here λ is the thermal conductivity and c_p is the specific heat at constant pressure. The law was developed for low Prandtl numbers with the goal of offering an accurate wall function for high-Re_t models. The authors derived Eq. 48 from the heat-flux conservation near the wall, without neglecting the turbulent thermal diffusivity K_h. The formulation does not need a blending function (such as that proposed by Kader 1981), which links the linear law close to the wall with the logarithmic further away from the wall. Equation 48 approaches $\Theta^+ = Pr\ z^+$ for small z^+, which fulfills the requirement of a laminar law in the near-wall region. The predicted mean temperature profile generally agrees with the law-of-the-wall for $z^+ < 200$, but the slope of both the algebraic and the differential heat-flux model is higher than the slope obtained with Eq. 48. Nevertheless, the proposed function of Duponcheel et al. (2014) could be a useful wall function for a high-Re_t heat transfer simulation of the Ekman layer.

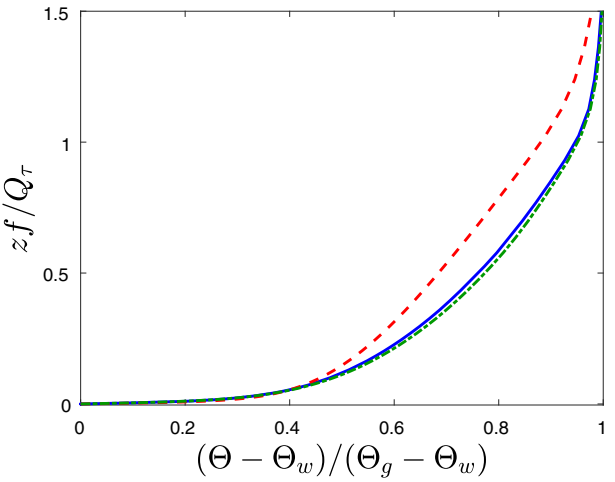

Fig. 10 Predicted vertical profiles of mean potential temperature. —— differential transport model; -·-·- non-linear model; - - - - - Fourier's law ($Pr_t = 0.85$)

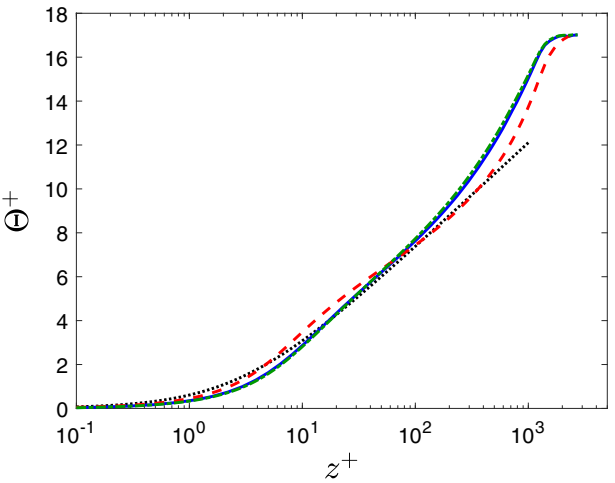

Fig. 11 Mean temperature profile in wall coordinates. —— differential transport model; -·-·- non-linear model; - - - - - Fourier's law; ····· law of the wall for temperature of Duponcheel et al. (2014) (Eq. 48 with $Pr = 0.71$, $Pr_t = 0.85$, $\kappa = 0.41$)

3.5 Turbulent Heat Fluxes

The predicted vertical profiles of the turbulent heat fluxes obtained with the various models are presented in Fig. 12. The fluxes are non-dimensionalized by the friction velocity and the friction temperature. It is interesting to note that the largest of the heat fluxes occurs in the streamwise direction ($\overline{u\theta}$) even though the only temperature gradient that is finite is in the vertical direction. The Fourier law cannot predict the conductive heat transfer, as the law does not consider velocity gradients and Reynolds stresses. At the same time, the maximum value of the vertical heat flux departs from the differential and algebraic models by $\approx 60\%$. The differential model and the algebraic model predict different maximum values of $-\overline{u\theta}$

and $-\overline{v\theta}$. However, the location of these maxima is the same. The difference between both models in the prediction of $-\overline{w\theta}$ is insignificant.

3.6 Eddy Viscosity, Diffusivity and the Turbulent Prandtl Number

Predicted and measured vertical profiles of the turbulent viscosity K_m are presented in Fig. 13. Plotted there is the single (isotropic) profile obtained with the $k-\epsilon$ model (Eq. 9), and two profiles that are implied in the RSM but that do not enter into the computations viz.

$$K_{m_{13}} = \frac{-\overline{uw}}{\partial U/\partial z}, \tag{50}$$

$$K_{m_{23}} = \frac{-\overline{vw}}{\partial V/\partial z}. \tag{51}$$

The discontinuous behaviour obtained for $K_{m_{23}}$ is characteristic of that obtained in a wall jet and arises because $\partial V/\partial z$ passes through zero. With increase in vertical distance, the eddy viscosities $K_{m_{13}}$ and $K_{m_{23}}$ move closer together suggesting that departures from isotropy are quite small. The isotropic eddy viscosity is seen to closely follow the $K_{m_{13}}$ distribution across a significant depth of the Ekman layer.

The components of eddy viscosity are sometimes presented in the literature not as individual components but in an averaged form. Marlatt et al. (2012) define the average viscosity as

$$K_m = \left[\overline{uw}^2 + \overline{vw}^2\right]^{0.5} \left[\left(\frac{\partial U}{\partial z}\right)^2 + \left(\frac{\partial V}{\partial z}\right)^2\right]^{-0.5}. \tag{52}$$

The profiles of the averaged eddy viscosity as deduced from the DNS results of Marlatt et al. (2012) and the experimental data of Caldwell et al. (1972) are presented in Fig. 13 (note that the Caldwell et al. (1972) results pertain to the somewhat higher Reynolds number of $Re_f = 1159$). Because the RSM predicted profiles of $K_{m_{13}}$ and $K_{m_{23}}$ are essentially identical, their individual profiles turn out to be essentially identical to the profile of their average as evaluated from Eq. 52. In the inner layer, remarkably close correspondence between the RSM and DNS results is observed though the RSM results do not capture the non-monotonic behaviour seen in the DNS results.

Profiles of the eddy diffusivity K_h are presented in Fig. 14. For the non-linear and differential models, this parameter is obtained from

$$K_h = \frac{-\overline{w\theta}}{\partial \Theta/\partial z}, \tag{53}$$

and is presented in Fig. 14 as a function of non-dimensional height. The differential and non-linear algebraic models yield closely-matched results that indicates that the diffusive and convective processes are relatively small. In contrast, Fourier's law, with a constant Prandtl number of 0.85, yields substantially different results. There are no DNS or experimental data to confirm these results. By using Eqs. 52 and 53, the turbulent Prandtl number can now be calculated using the models predictions. The results are shown in Fig. 15 where it can be seen that the models indicate that the turbulent Prandtl number depends on height, especially in the near-wall region ($zf/Q_\tau < 0.05$), with average values that can exceed 1.1. This finding is in good accord with results from several semi-empirical models for the near-wall behaviour of turbulent Prandtl number in laboratory flows (Kays et al. 2005). Li (2019) reviewed alternative models for the turbulent Prandtl number in the neutral ABL and

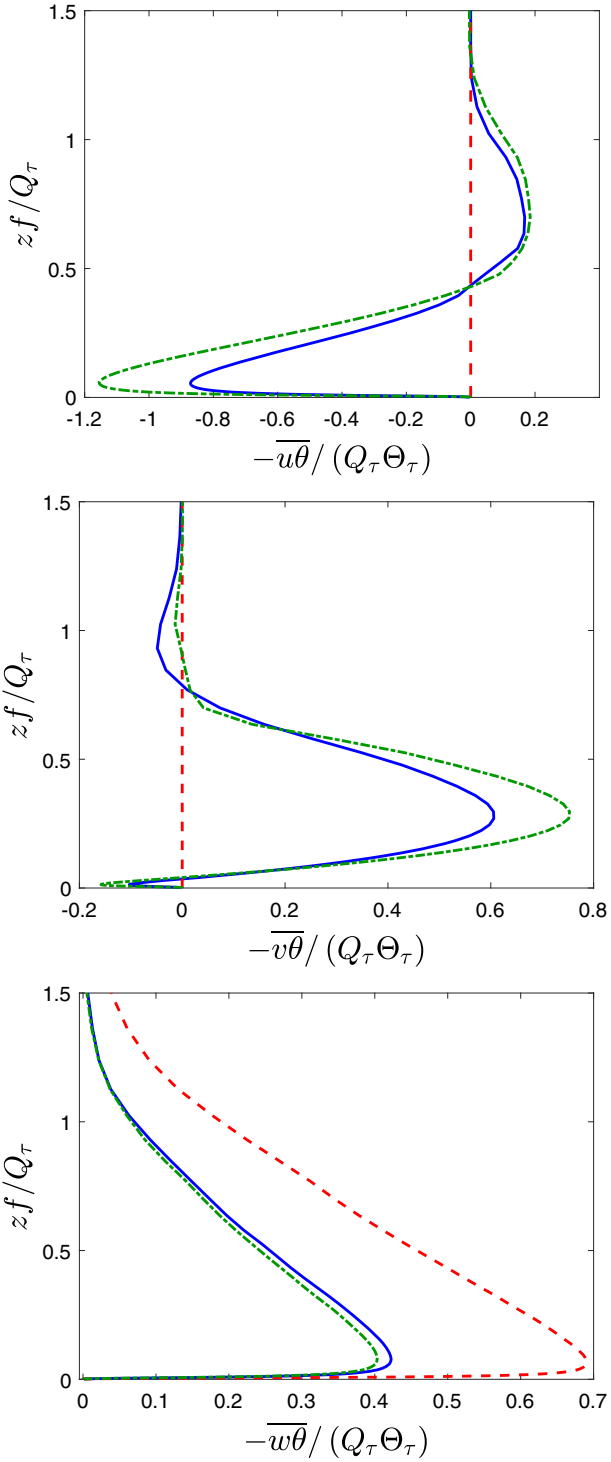

Fig. 12 Turbulent heat fluxes. differential transport model; non-linear model; Fourier's law

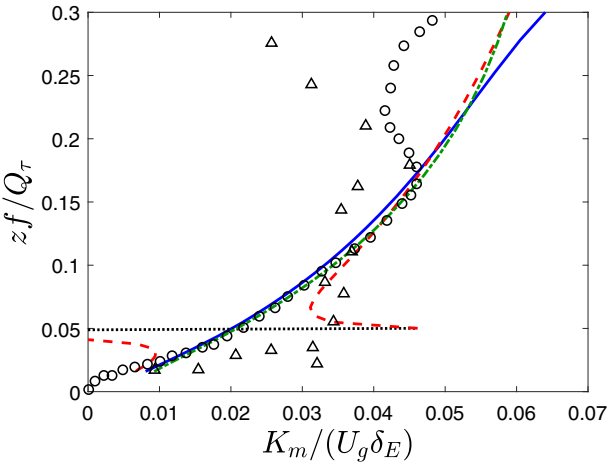

Fig. 13 Vertical profiles of eddy viscosity. ——— high-Re_t model $K_{m_{13}}$; - - - - high-Re_t model $K_{m_{23}}$; -·-·- $k-\epsilon$ model; ◯ DNS results of Marlatt et al. (2012); △ experimental data of Caldwell et al. (1972) ($Re_f = 1159$)

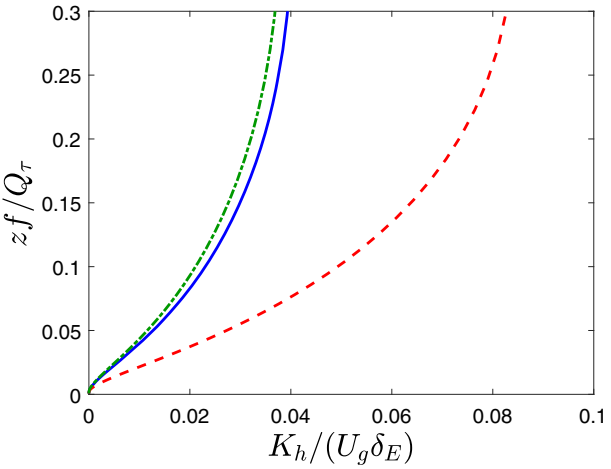

Fig. 14 Vertical profiles of eddy diffusivity. ——— differential transport model; -·-·- non-linear model; - - - - Fourier's law

found that different theories yield values that are higher than 0.85. Repeating the Fourier law calculations with $Pr_t = 1.0$ produced temperature profiles that were virtually identical to the those obtained with the differential and the non-linear models.

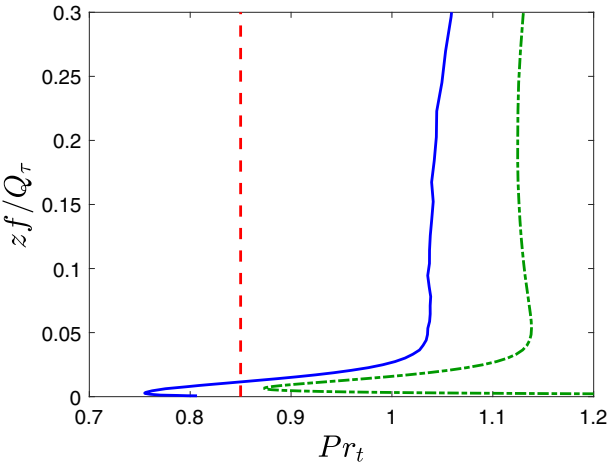

Fig. 15 Turbulent Prandtl number as a function of height above surface. ——— differential transport model; -·-·- non-linear model; - - - - $Pr_t = 0.85$

4 Conclusions

The turbulent Ekman layer provides a simple model for the ABL and hence the interest in developing turbulent closures that can accurately predict its flow and thermal fields. The results presented above indicate that the $k - \epsilon$ turbulence model, in its standard form, can be relied upon to capture the main features of this flow such as the vertical distribution of the mean velocity components. When presented in wall coordinates, these model results accurately reproduce the logarithmic-law profile obtained from the DNS results of Marlatt et al. (2012). The geostrophic drag coefficient was also well predicted with this model. Because attention here was confined to fully-developed flow, the normal stresses obtained by the Boussinesq assumption are obtained as being equal whereas in reality turbulence is highly anisotropic due to the damping effects of the surface. On the other hand, the turbulent shear stresses were reasonably well predicted.

Concerning the Reynolds-stress transport models, results obtained with high- and low-Re_t variants of the same basic model were quite similar for the vertical profiles of the mean velocity components and the Reynolds stresses. The use of the logarithmic law-of-the-wall to provide boundary conditions for the high-Re_t model does not appear to have adversely affected its overall performance, though having to apply these conditions at some distance away from the surface meant that only the low Re_t model was capable of reproducing the entire Ekman spiral. Examination of the predicted directions of the resultant turbulent shear stresses and the associated gradients of mean velocity gradients showed these to be coincident across the vertical extent of the Ekman layer. Furthermore, analysis of the predicted vertical profiles of the eddy viscosities $K_{m_{13}}$ and $K_{m_{23}}$ showed these to be reasonably equal except for a small region close to the surface where $K_{m_{23}}$ was discontinuous where the lateral velocity component V was at a maximum and hence $\partial V/\partial z$, which appears in the denominator, was identically zero. This result indicates that the assumption of isotropic eddy viscosity in lower-order models such as the $k - \epsilon$ is quite acceptable in this flow.

Even though the focus of the study was on the case of $Re_f = 1000$ and a latitude of 90° N, the conditions for which the majority of DNS results are available, the results obtained with the low-Re_t model were used to in conjunction with the similarity theory of Spalart (1989) to obtain predictions at Re_f values more representative of those encountered in the ABL. Subsequent predictions with the low-Re_t model for values of Re_f up to 40, 000 agreed very well with extrapolated similarity theory results.

For weather predictions, the computational cost of turbulence models is an important parameter. Since the high Re_t model yields as good results as the low Re_t alternative but with less computational cost, there is no justification for using the more complex and computationally more demanding model. However, if the simulation of flow very close to the surface is of interest, then the only available option would be to perform the calculations directly to the wall.

The thermal field predictions obtained with a non-linear algebraic heat-flux model and the more complex differential transport model showed no significant differences in terms of the vertical profiles of the mean temperature and the heat fluxes. In contrast, Fourier's law, even when used in conjunction with the Reynolds-stress model, produced a temperature distribution that is vastly different from the other models. These model results can be brought in line with the others simply by assigning to the turbulent Prandtl number a value of 1 instead of its more usual value of 0.85.

Acknowledgements Lukas Braun gratefully acknowledges the financial support provided by the Studienstiftung des deutschen Volkes that facilitated this research at UC Davis.

Appendix: Comparisons with the DNS of Deusebio et al. (2014)

A reviewer drew our attention to the DNS results of Deusebio et al. (2014) for the mean temperature and vertical heat flux in a neutrally-stratified Ekman layer. These results are presented in Fig. 16 where they are compared with the present predictions. In the viscous sub-layer ($z^+ < 8$), the correspondence between the DNS results for mean temperature and the predictions of the differential and the non-linear flux models is quite close. However, differences appear further away from the surface. There, the pronounced change in the slope of the temperature profile exhibited by the DNS is not reproduced in the models' predictions. Concerning the vertical turbulent heat flux, significant differences between the present results and the DNS are apparent. We are at a loss to explain the observed differences in the profiles shape, especially in the outer region of the boundary layer where the DNS results show an extensive region of constant heat flux. We are however encouraged to see that the two models yield almost identical results even though they differ in so many ways (e.g. algebraic vs. differential), and share no assumptions in their formulation.

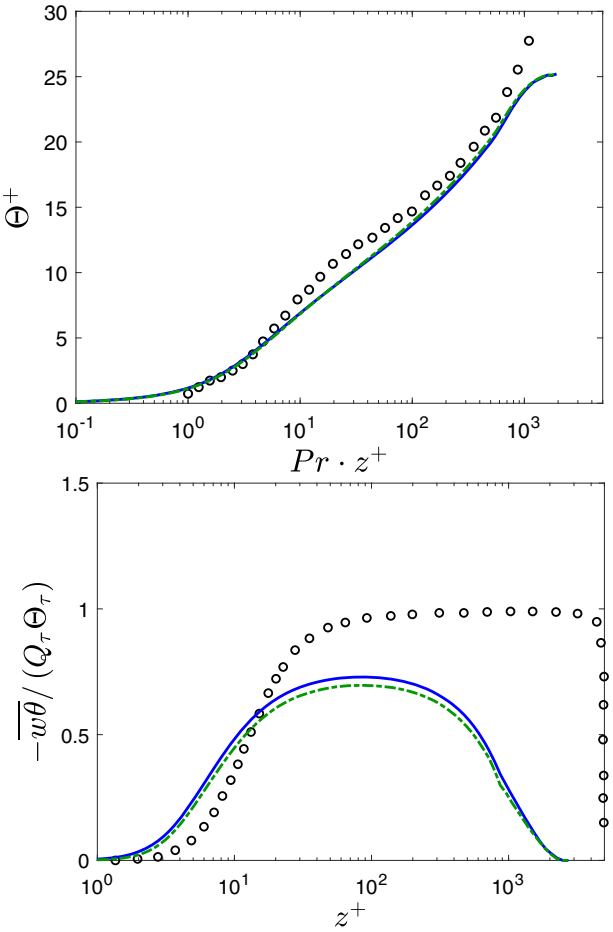

Fig. 16 DNS and present predictions of mean temperature (top) and vertical heat flux ($Re = 1600$). ◯ DNS of Deusebio et al. (2014); ——— differential transport model; -·-·- non-linear model

References

Andrén A (1991) A TKE-dissipation model for the atmospheric boundary layer. Boundary-Layer Meteorol 56:207–221

Apsley DD, Castro IP (1997) A limited-length-scale k-ϵ model for the neutral and stably stratified atmospheric boundary layer. Boundary-Layer Meteorol 83(1):75–98

Brost RA, Wyngaard JC, Lenschow DH (1982) Marine stratocumulus layers. Part II: turbulence budgets. J Atmos Sci 39:818–836

Caldwell DR, van Atta CW, Helland KN (1972) A laboratory study of the turbulent Ekman layer. Geophys Fluid Dyn 3(1):125–160

Coleman GN (1999) Similarity statistics from a direct numerical simulation of the neutrally stratified Planetary Boundary Layer. J Atmos Sci 56(6):891–900

Coleman GN, Ferziger JH, Spalart PR (1990) A numerical study of the turbulent Ekman layer. J Fluid Mech 213:313–348

Csanady GT (1967) On the "resistance law" of a turbulent Ekman layer. J Atmos Sci 24:467–471

Cushman-Roisin B, Beckers JM (2010) Introduction to geophysical fluid dynamics. Pearson Education, London

Daly BJ, Harlow FH (1970) Transport equations in turbulence. Phys Fluids 13(11):2634–2649
Detering HW, Etling D (1985) Application of the E-ϵ turbulence model to the atmospheric boundary layer. Boundary-Layer Meteorol 33(2):113–133
Deusebio E, Brethouwer G, Schlatter P, Lindborg E (2014) A numerical study of the unstratified and stratified Ekman layer. J Fluid Mech 755:672–704
Duponcheel M, Bricteux L, Manconi M, Winckelmans G, Bartosiewicz Y (2014) Assessment of RANS and improved near-wall modeling for forced convection at low Prandtl numbers based on LES up to Re=2000. Inl J Heat Mass Transf 75:470–482
Gibson MM, Launder BE (1978) Ground effects on pressure fluctuations in the atmospheric boundary layer. J Fluid Mech 86(3):491–511
Irwin HPAH (1973) Measurements in a self-preserving plane wall jet in a positive pressure gradient. J Fluid Mech 61:33–63
Johnstone JP, Flack KA (1996) Review—advances in three-dimensional turbulent boundary layers with emphasis on the wall-layer regions. J Fluids Eng 118:219–232
Kader BA (1981) Temperature and concentration profiles in fully turbulent boundary layers. Int J Heat Mass Transf 24(9):1541–1544
Kannepalli C, Piomelli U (2000) Large-eddy simulation of a three-dimensional shear-driven turbulent boundary layer. J Fluid Mech 423:175–203
Kays W, Crawford M, Weigand B (2005) Convective heat and mass transfer, 4th edn. McGraw Hill, New York
Kays WM (1994) Turbulent Prandtl number—where are we? J Heat Transf 116(2):284–295
Kebede W, Launder BE, Younis BA (1985) Large-amplitude periodic pipe flow: a second-moment closure study. In: 5th symposium on turbulent shear flow, pp 1623–1629
Launder BE (1976) Heat and mass transfer, Chap. 6. In: Bradshaw P (ed) Turbulence, vol 12. Topics in applied physics. Springer, Berlin, pp 231–287
Launder BE, Spalding DB (1972) Lectures in Mathematical models of turbulence. Academic Press, London
Li D (2019) Turbulent Prandtl number in the atmospheric boundary layer—where are we now? Atmos Res 216:86–105
Malin MR, Younis BA (1990) Calculation of turbulent buoyant plumes with a Reynolds stress and heat flux transport closure. Int J Heat Mass Transf 33(10):2247–2264
Marlatt S, Waggy S, Biringen S (2012) Direct numerical simulation of the turbulent Ekman layer: evaluation of closure models. J Atmos Sci 69:1106–1117
Mauritsen T, Svensson G, Zilitinkevich SS, Esau I, Enger L, Grisogono B (2007) A total turbulent energy closure model for neutrally and stably stratified atmospheric boundary layers. J Atmos Sci 64:4113–4126
Miyashita K, Iwamoto K, Kawamura H (2006) Direct numerical simulation of the neutrally stratified turbulent Ekman boundary layer. J Earth Simulator 6:3–15
Momen M, Bou-Zeid E (2017) Mean and turbulence dynamics in unsteady Ekman boundary layers. J Fluid Mech 816:209–242
Müller H, Younis BA, Weigand B (2015) Development of a compact explicit algebraic model for the turbulent heat fluxes and its application in heated rotating flows. Int J Heat Mass Transf 86:880–889
Schlichting H, Gersten K (2006) Grenzschicht-Theorie, 10th edn. Springer, Berlin
Sogachev A, Kelly M, Leclerc MY (2012) Consistent two-equation closure modelling for atmospheric research: buoyancy and vegetation implementations. Boundary-Layer Meteorol 145:307–327
Sous D, Sommeria J (2012) A Tsai's model based S-PIV method for velocity measurements in a turbulent Ekman layer. Flow Meas Instrum 26:102–110
Spalart PR (1989) Theoretical and numerical study of a three-dimensional turbulent boundary layer. J Fluid Mech 205:319–340
Spalart PR, Coleman GN, Johnstone R (2008) Direct numerical simulation of the Ekman layer: a step in Reynolds number, and cautious support for a log law with a shifted origin. Phys Fluids 20(10):101507
Wilcox DC (1993) Turbulence modeling for CFD. DCW Industries Inc, La Cãnada
Wirth A (2010) On the Ekman spiral with an anisotropic eddy viscosity. Boundary-Layer Meteorol 137(2):327–331
Younis BA (1987) EXPRESS: a computer programme fortwo-dimensionalturbulent boundary layer flows. Department of CivilEngineering, City University, London
Younis BA, Speziale CG, Berger SA (1998) Accounting for the effects of system rotation on the pressure-strain correlation. AIAA J 36(9):1746–1748

Younis BA, Speziale CG, Clark TT (2005) A rational model for the turbulent scalar fluxes. Proc R Soc A Math Phys Eng Sci 461(2054):575–594

Younis BA, Weigand B, Laqua A (2012) Prediction of turbulent heat transfer in rotating and nonrotating channels with wall suction and blowing. J Heat Transf 134(7):071702